JACS
JOURNAL OF THE AMERICAN CHEMICAL SOCIETY

ARTICLE

pubs.acs.org/JACS

Controlling Assembly of Paired Gold Clusters within Apoferritin Nanoreactor for in Vivo Kidney Targeting and Biomedical Imaging

Cuiji Sun,[†,‡,#] Hui Yang,[†,#] Yi Yuan,[§,#] Xin Tian,[†] Liming Wang,[†] Yi Guo,[‡] Li Xu,[*,‡] Jianlin Lei,[§] Ning Gao,[§] Gregory J. Anderson,[∥] Xing-Jie Liang,[†] Chunying Chen,[†] Yuliang Zhao,[*,†,⊥] and Guangjun Nie[*,†]

[†]CAS Key Laboratory for Biological Effects of Nanomaterials & Nanosafety, National Center for Nanoscience and Technology, Beijing 100190, China

[‡]Key Laboratory for Molecular Enzymology and Engineering, the Ministry of Education, Jilin University, Changchun, China

[§]MOE Key Laboratory of Bioinformatics, Center for Structural Biology, School of Life Sciences, Tsinghua University, Beijing, China

[∥]Iron Metabolism Laboratory, Queensland Institute of Medical Research, Royal Brisbane Hospital, Brisbane, Queensland 4029, Australia

[⊥]CAS Key Laboratory for Biological Effects of Nanomaterials & Nanosafety, Institute of High Energy Physics, Chinese Academy of Sciences, Beijing, China

Supporting Information

ABSTRACT: Functional nanostructures with high biocompatibility and stability, low toxicity, and specificity of targeting to desired organs or cells are of great interest in nanobiology and medicine. However, the challenge is to integrate all of these desired features into a single nanobiostructure, which can be applied to biomedical applications and eventually in clinical settings. In this context, we designed a strategy to assemble two gold nanoclusters at the ferroxidase active sites of ferritin heavy chain. Our studies showed that the resulting nanostructures (Au−Ft) retain not only the intrinsic fluorescence properties of noble metal, but gain enhanced intensity, show a red-shift, and exhibit tunable emissions due to the coupling interaction between the paired Au clusters. Furthermore, Au−Ft possessed the well-defined nanostructure of native ferritin, showed organ-specific targeting ability, high biocompatibility, and low cytotoxicity. The current study demonstrates that an integrated multimodal assembly strategy is able to generate stable and effective biomolecule−noble metal complexes of controllable size and with desirable fluorescence emission characteristics. Such agents are ideal for targeted in vitro and in vivo imaging. These results thus open new opportunities for biomolecule-guided nanostructure assembly with great potential for biomedical applications.

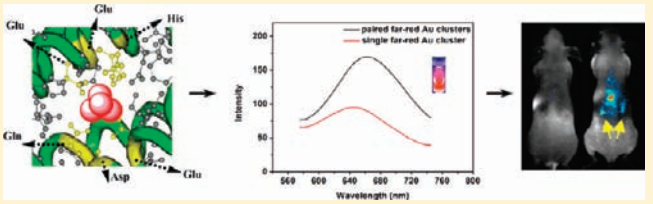

INTRODUCTION

Various nanostructures have shown great promise in biomedical imaging, biosensing, drug delivery, and disease diagnostics.[1−3] Gold clusters (Au clusters) below 2 nm in diameter have attracted great attention due to their unique physiochemical properties, such as intrinsic photoluminescence[4,5] and selective catalytic activities.[6,7] In addition, Au clusters are stable, even under extremely acidic or basic conditions, and maintain their specific topological structures. Therefore, Au clusters hold great promise for biomedical imaging[5,8] and diagnosis.[5,9] However, traditional routes (chemical and physical methods) of Au clusters synthesis are complicated and difficult to control. For the chemical methods, Au ions are first heated in organic solutions with high speed stirring, followed by the addition of reductants and stabilizers to allow the rapid formation of small Au clusters. This chemical reduction reaction requires multiple steps and high energy consumption and leads to the formation of complex products that may require further purification.[10−13] The physical method involves laser vaporization, which generates a range of byproduct and necessitates further purification to obtain pure Au clusters.[14] Because of the small size of Au clusters, they are not readily applicable to specific tissue or cell targeting in biomedical applications. Furthermore, the quantum yield of Au clusters synthesized with the traditional methods is low (less than 6%),[15] which means that their fluorescence intensity is not strong enough for biomedical imaging.

Proteins are native nanoscale structures with unique, defined three-dimensional structures and biological functions. The integration of noble metal clusters and proteins may create novel nanostructures with great potential for biomedical applications. Ferritins are composed of 24 subunits of two types, the heavy chain (H-ferritin) and light chain (L-ferritin), arranged in a cubic symmetry to produce a hollow nanocage 12 nm in diameter with an 8 nm cavity (Figure 1a).[16] Physiologically, ferritins are ubiquitous cellular iron storage and detoxification proteins. Within the ferritin nanocage, ferrous iron ion is oxidized by the ferroxidase center of H-ferritin, and the resulting mineral form is stored inside the protein shell. The ferroxidase center is composed of six amino acid residues, one histidine (His), one aspartic acid (Asp), one glutamine (Gln), and three glutamic acids (Glu). In the current study, we chose

Received: January 25, 2011
Published: May 04, 2011

dx.doi.org/10.1021/ja200746p | J. Am. Chem. Soc. 2011, 133, 8617–8624

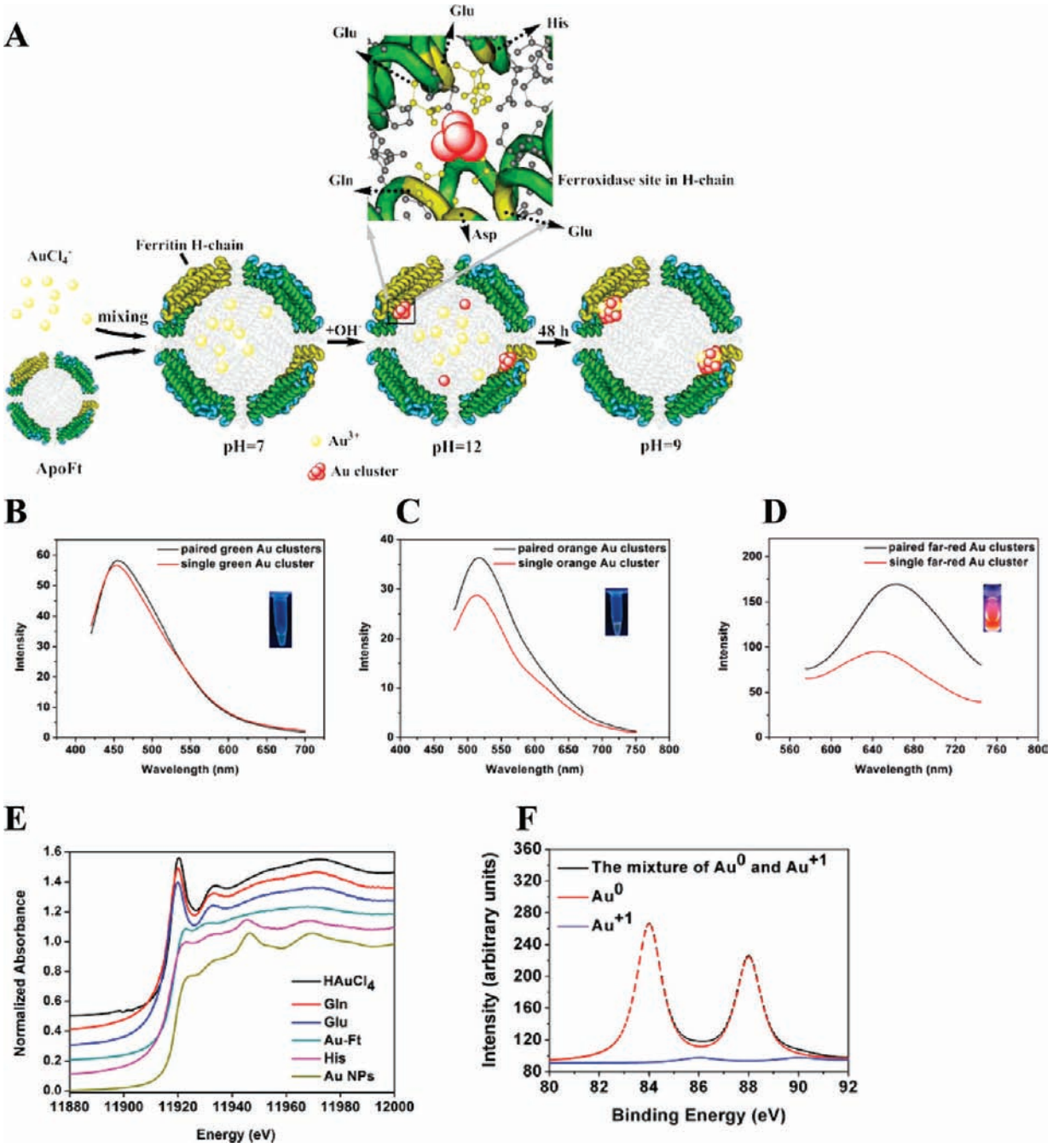

Figure 1. Schematic illustration of the synthesis route and optical properties of Au−Ft. (a) Schematic illustration of the synthesis of Au−Ft. The His residues at the ferroxidase centers play an important role in the in situ Au cluster assembly. The emission spectra are for green (b), orange (c), and far-red (d) Au−Ft, respectively. The insets were the images of various Au−Ft samples under UV-light excitation. (e) XANES spectra showing the Au chemical composition and possible binding with His residues. Au nanoparticles (Au^0) and $HAuCl_4$ (Au^{3+}) were adopted as model samples. Mixtures of Glu, Gln, and His with $HAuCl_4$ and Au−Ft double far-red clusters were chosen to study Au speciation. (f) Au 4f electron region of the X-ray photoelectron spectrum (XPS) of far-red Au−Ft. Approximately 5.3% of the Au is on the surface of the Au-cluster as Au^{1+}. Black line, Au $4f_{7/2}$ spectrum; red line, binding energy of 84.0 eV; blue line, binding energy of 86 eV.

ferritin isolated from horse spleen, which, on average, is composed of 22 L-ferritin and 2 H-ferritin subunits.[16,17] Because of the strong binding of Au^{3+} to the imidazole ring of the His residues at the ferroxidase center of H-ferritin, we utilized the hisdines as "points of control"[18−21] to grow Au cores.[22] Because each ferritin nanocage has two ferroxidase centers, a pair of Au clusters can be assembled in each complex. The spatial limitation of the local microenvironment of the ferroxidase centers controls the size and shape of the Au clusters. To further precisely control the process of Au clusters assembly, a weak reductant must be used to allow the assembly reaction to be processed slowly and in a controlled manner. More importantly, the pair of Au clusters within a ferritin shell may interact with each other, and the coupling between the Au clusters may enhance the fluorescence properties of the Au clusters. For example,

dx.doi.org/10.1021/ja200746p |J. Am. Chem. Soc. 2011, 133, 8617–8624

the coupling between two close quantum dots achieves strong fluorescent intensity, and a red shift in the emission has been reported.[23−26] The enhanced fluorescence intensity and far-red or near-infrared emission are ideal for biological imaging applications. They are especially suitable for whole body imaging applications where low background autofluorescence and enhanced tissue penetration are desirable characteristics.[27] In this study, we designed a synthesis strategy termed "points of control", in which the apoferritin (apoFt) protein cage was used as a nanoreactor to facilitate controllable Au cluster formation at the ferroxidase enzymatic center of the heavy chain of ferritin. The resulting Au cluster−ferritin nanostructure has been used successfully for both in vitro and in vivo molecular targeting and imaging.

EXPERIMENTAL SECTION

Preparation of Au−Ft. $HAuCl_4$ (150 μL; 5 mM) was added to 150 μL of horse spleen apoFt (49 mg/mL) (Sigma-Aldrich). After the mixture was shaken and mixed for 2 min, 10 μL of 1 M NaOH was added to the solution, followed by incubation for 6, 12, or 36 h at 37 °C. After the green, orange, and far-red Au-Ft were formed, the reaction solution was ultrafiltered with a centrifugal filter device (Amicon Ultra-15; 30 000 molecular weight cutoff) and washed three times with 3 mL of double distilled water. The concentration of apoFt protein was measured by the bicinchoninic acid method (BCA).

The Quantum Yield of Au−Ft. The quantum yield (QY) of Au−Ft was determined by measuring the integrated fluorescence intensities of the Au−Ft and the reference compound (rhodamine 6G in basic ethanol, QY = 95%) under 470 nm excitation with LS55 fluorescence spectrometry.[28]

Cryo-electron Microscopy. An aliquot of 3.5 μL of diluted sample (~7.2 mg/mL protein, distilled with distilled water) was applied to a 300 mesh glow-discharged Quantifoil 2/4 grid, blotted inside an FEI Vitrobot at room temperature, and plunged into liquid ethane. The specimen was examined at liquid nitrogen temperature in an FEI Titan Krios cryo-electron microscope operated at 300 kV using a nominal magnification of 59 000×. Images were recorded on an FEI Eagle 4k × 4k CCD camera under low-dose conditions with a dose of ~20 $e^-/Å^2$ and had a pixel size of ~1.5 Å on the object scale.

High-Resolution Transmission Electron Microscopy (HRTEM) and High-Angle Annular Dark Field Scanning Transmission Electron Microscopy (HAADF-STEM). An aliquot of 4 μL of far-red Au-Ft (360 nM) was applied to a glow-discharged grid coated with a layer of amorphous carbon film, and excess fluid was gently blotted off with filter paper. The HAADF-STEM and HRTEM images were recorded on an FEI Tecnai F20 U-TWIN electron microscope.

X-ray Photoelectron Spectroscopy (XPS). The oxidation state of the Au clusters was determined by XPS. Narrow-scan XPS spectra of Au $4f_{7/2}$ were deconvoluted by the XPSPEAK software (Version 4.1) using adventitious carbon to calibrate the binding energy of C1s (284.8 eV).

Chemical Speciation Analysis with XANES. XANES of gold was measured at the Shanghai Synchrotron Radiation Facility (SSRF), China. XANES spectra of the gold LIII edge were recorded at BL14W1 and were normalized with Win XAS 3.1.

Cell Viability and Cytotoxicity Assays. For viability assays, Caco-2 and HepG2 cells (American Type Culture Collection (ATCC), Manassas, VA) were seeded at a density of 6×10^4 cells/well in 24-well plates for 12 h. The medium was replaced with 400 μL of medium containing a series of concentrations of either apoFt or far-red Au-Ft. After 12 h incubation, the numbers of viable and total cells were quantified using a Vi-CELL XR Cell Viability Analyzer (Beckman Coulter, Brea, CA).

Cell Imaging of Far-Red Au−Ft. The intrinsic fluorescence of Au−Ft was used to monitor its cellular uptake. Caco-2 and HepG2 cells were incubated with far-red Au−Ft for 12 h. The cells were imaged on a Nikon Ti-e microscope with an UltraVIEW Vox confocal attachment (Perkin-Elmer). The excitation/emission wavelengths were 488 nm/615 nm for Au−Ft.

In Vivo and ex Vivo Imaging with Far-Red Au−Ft. Nu/nu female mice (8 weeks, 20 ± 2 g) obtained from Beijing Vital River Laboratories were injected via the tail vein with the Au-Ft probe (0.8 nmol/g body weight) diluted in 0.9% NaCl solution. In vivo fluorescence images of the mice were obtained with a Maestro in vivo spectrum imaging system (Cambridge Research & Instrumentation, Woburn, MA). The excitation filter was set as 576−621 nm; the emission filter was a 635 nm long-pass filter. The liquid crystal tunable emission filter (LCTF, with a bandwidth of 20 nm and a scanning wavelength range of 500−950 nm) was automatically stepped in 10 nm increments from 630 to 800 nm, while the CCD captured images at each wavelength with constant exposure. At the special time points of 0, 1, 2, 4, and 7 h after injection, the mice were sacrificed, and the organs were removed for ex vivo fluorescence imaging on the same spectrum imaging system. All animal experiments were approved by the Animal Ethics Committee of the Medical School, Beijing University. The tissue slides were examined via an inverted fluorescence microscope (MD2500-3HF-FL, Leica Microsystems, Wetzlar, Germany) equipped with a Nuance multispectral imaging system (CRi, Woburn, MA). To obtain the Au−Ft signal, excitation and emission filters were set at 535 ± 25 nm and 590LP, respectively; for DAPI signal, the excitation and emission filters were set at 350 ± 25 nm and 420LP, respectively.

ICP-MS. Far-red Au−Ft tissue distribution was assessed by measuring Au levels by ICP-MS (Elemental X7, Thermo Electron). Tissues were removed, washed, and weighed. For each sample, 30−50 mg of tissue was digested in nitric acid and heated at 120 °C for several hours. Hydrogen peroxide solution was used to drive off the vapor of nitrogen oxides until the solution was colorless and clear. After the solution volume was adjusted to 2 mL using 2% nitric acid and 1% hydrochloride acid, the Au content was analyzed using ICP-MS. Indium (20 ng/mL) was used as an internal standard.

RESULTS AND DISCUSSION

It is crucial to find an appropriate weak reductant to fine-tune the assembly of Au pairs within the ferritin shell. It is well-known that elemental Au can be dissolved in aqua regia to generate Au^{3+}. We speculate that we may use the reverse reaction to form Au clusters from Au^{3+} by changing the reaction pH to basic. Through calculating the standard oxidation−reduction potentials of Au ions, elemental Au, and OH^-, we have determined that 12 M OH^- could reduce 4 M Au^{3+} and release 2.799 $E°$/V of energy.[29,30] The reactions shown in standard electrode potentials among Au^{3+}, Au^{1+}, and Au^0 can be simplified as follows (electrode process, $E°$/V):

$$(1)\ O_2 + 2H_2O + 4e^- \rightarrow 4OH^-, 0.401$$

$$(2)\ AuCl_4^- + 3e^- \rightarrow Au + 4Cl^-,\ 1.002$$

Reactions (1) and (2) lead to:

$$(3)\ 4AuCl_4^- + 12OH^- \rightarrow 3O_2 + 6H_2O + 4Au + 16Cl^-,\ 2.799$$

As shown in reaction (3), at basic pH, the tendency of Au^{3+} to be reduced to Au^0 or Au^{1+} is significantly increased (the higher is the reduction potential, the easier is the reduction).

To avoid apoFt subunit dissociation under acidic conditions, the reaction substrate ($HAuCl_4$) was first adjusted to pH 7 before mixing with various molar ratios of apoFt. The molar ratio of Au

dx.doi.org/10.1021/ja200746p | J. Am. Chem. Soc. 2011, 133, 8617–8624

ions to apoFt determines the size of the resulting Au clusters. We chose three different molar ratios of apoFt/$HAuCl_4$ (1:16, 1:26, and 1:50). The mixtures were kept at 37 °C for 15 min to allow Au ions to adsorb onto the nucleation points (His residues). The His residues may partially reduce Au^{3+}, which in turn may enhance the binding affinity of Au ions. The reaction mixture was then adjusted to pH 12 and kept for 5, 12, or 24 h. The pH of each reaction mixture was approximately 9 at the end of the reactions. A schematic illustration of the whole assembly reaction is shown in Figure 1a. The tunable fluorescent emissions of the Au ferritin clusters (Au−Ft) are shown in Figure 1b−d. With increasing Au/apoFt ratio, the size of the Au clusters increased as demonstrated by the red shift in the fluorescent emissions (from green to orange to near-red emission) following UV excitation (Figure 1b−d and the insets). The analysis of the fluorescent excitation and emission spectra indicated that the maximal emission peaks of Au−Ft pairs were 454, 516, and 665 nm, corresponding to excitations at 385, 455, and 470 nm, respectively. The excitation and absorption spectra of the three types of Au clusters were shown in Figure S1.

To confirm the pivotal roles of His residues of H-ferritin in the "points of control" synthesis of Au−Ft, we examined the interactions of His, Glu, and Gln with Au^{3+}. When His, Glu, and Gln were mixed in a 1:1 molar ratio with Au^{3+} for 2 days, only His induced Au^{3+} to form purple aggregates, which indicated the reduction of Au^{3+} to Au, while no interreactions with Glu or Gln were observed. The oxidation state of Au was further characterized by synchrotron radiation-based X-ray absorption near edge structure spectroscopy (XANES) (Figure 1e). The Au atom in $HAuCl_4$ represents Au^{3+}, and its characteristic peak appeared predominantly at 11 920 eV. Mixtures of Glu and Gln with $HAuCl_4$ showed spectra similar to that of Au^{3+}, indicating that both Glu and Gln did not reduce Au^{3+} under the current experimental conditions. In contrast, Au nanoparticles (3 nm in diameter, capped with 2-[2-(2-mercaptoethoxy)ethoxy]ethanol) showed peaks characteristic of elemental Au (Au^0) with maximum intensities at 11 944 and 11 965 eV (Figure 1e). A mixture of His and $HAuCl_4$ showed an XANES (X-ray absorption near edge structure) spectrum, almost identical to that of Au nanoparticles. This similarity suggests that His could reduce Au^{3+} to Au^0. Interestingly, chemical speciation analysis showed that the spectrum of far-red Au−Ft was very similar to that of the His and $HAuCl_4$ mixture, with a slightly weaker peak at 11 944 eV. Taken together, these results suggest that the oxidation state of Au in the apoFt nanoreactor is mainly as Au^0, mixed with a small percentage of Au ions, most likely Au^{1+}, but not Au^{3+} (Figure 1e). The oxidation state of the Au in the Au−Ft clusters was further quantitatively determined by X-ray photoelectron spectroscopy (XPS). The Au $4f_{7/2}$ spectrum (Figure 1f, black line) could be deconvoluted into two distinct components centered at binding energies of 84.0 (red line) and 86 eV (blue line),[31] which could be readily assigned to Au^0 and Au^{1+}, respectively. By comparing the area under each of the component lines, approximately 5.3% of Au^{1+} was present on the surface of the Au cluster (Figure 1f). The interaction between the Au^{1+} and Au^0 core might be weak, as the sharp decrease of the absorption spectra actually suggests that the contribution of Au^{1+} to the optical properties of the Au−Ft complex is minimal. The Au ion may play a role in binding the His in the ferritin interior cage.

The use of apoFt with two H subunits enabled the assembly of two Au clusters within the same protein nanoreactors, and this conferred some important and desirable characteristics on the complex. Coupling of excitations may occur between the pairs of

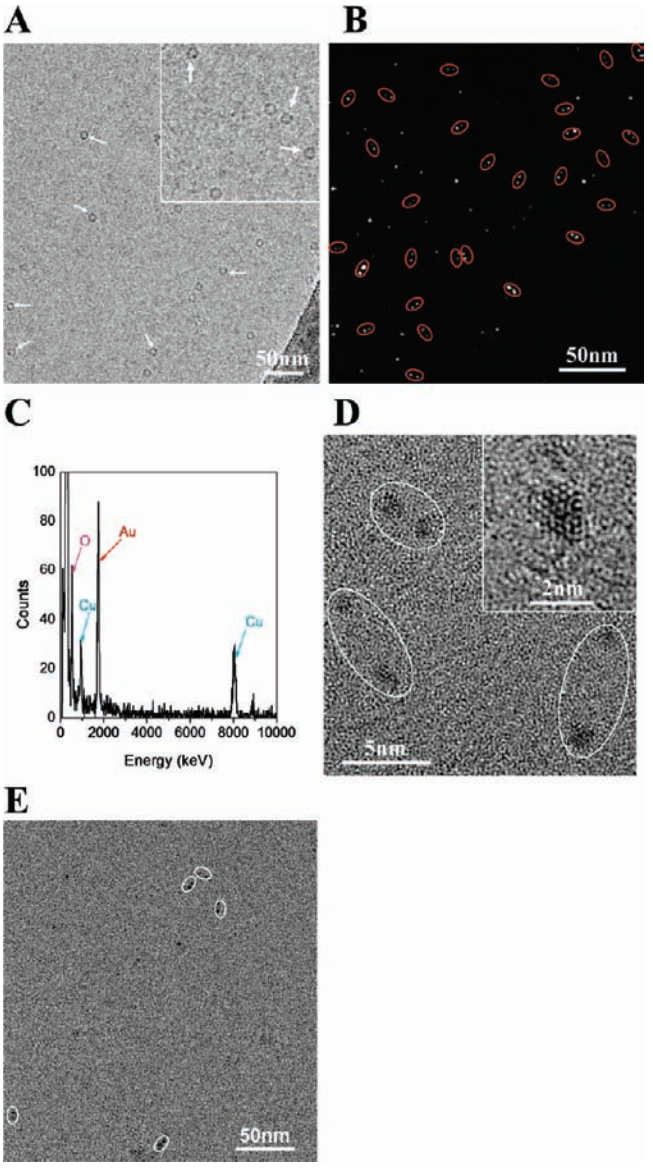

Figure 2. Characterization of far-red Au−Ft. (a) Cryo-electron microscopy (Cryo-EM) image. Paired Au clusters were observed within the ferritin nanoreactor (indicated by arrows). (b) HAADF-STEM image of far-red Au−Ft. There are about 40 paired Au clusters (indicated by ovals) within every 8 nm zone. (c) EDS of far-red Au−Ft showing the presence of elemental Au, but not iron in the nanostructure. (d) HRTEM image showing Au clusters at higher resolution. The crystal lattice spacing is about 0.22 nm (inset), and the 111 face of Au is evident. (e) TEM image of far-red Au−Ft showing that Au clusters exist as pairs, indicated by ovals.

Au clusters through two different mechanisms (electron exchange transfer or Forster resonance energy transfer, FRET), and this is dependent on the distance between the two clusters.[23−25,32] The interaction between the paired Au clusters in close proximity improves the optical properties of the Au cluster and makes them suitable for whole body fluorescence imaging. To confirm that we have synthesized a pair of Au clusters within a single ferritin nanoreactor, we dissociated the Au−Ft complex to single subunits by reducing the pH to 2 as previously described.[33] As expected, two of the 24 subunits contained a single Au clusters. By comparing the optical properties between the single and paired Au clusters, we

could directly observe the resonance energy transfer and quantitatively measure interactions between pairs of Au clusters by measuring the shift in maximal emission peaks and changes of fluorescence intensities. When excitation was carried out at 385 nm, for green Au−Ft, we observed a 2 nm red shift in the maximal emission peaks, from the single (452 nm) to the paired Au clusters (454 nm), and there was a weak increase in fluorescence intensity for the paired clusters (Figure 1b). When excitation was carried out at 455 nm for the orange Au−Ft, we observed a 3 nm red shift of maximal emission peaks from the single to the paired Au clusters and a 25% increase in fluorescence intensity for the paired clusters (Figure 1c). Interestingly, when 470 nm was chosen to excite the far-red Au−Ft, we observed a 20 nm red shift of maximal emission peaks from single to the paired Au clusters and 100% increase in fluorescence intensity for the paired clusters with a maximal emission at 665 nm (Figure 1d). The interior diameter of ferritin is about 8 nm. As the Au clusters increase in size, the distance between the two clusters is reduced. When a critical distance is reached, as in the far-red Au clusters (about 6 nm, Figure 2b), a FRET effect may occur and lead to the enhanced fluorescence emission and a red-shift of maximal emission (Figure 1d). Hence, we speculated that FRET effect may be a possible mechanism to explain the interactions between the paired Au clusters, although a significant decrease in the pH of the single Au cluster solution may interfere with fluorescence intensity.

Increased fluorescence intensity and the far-red to infrared fluorescence window are the two most desirable features for whole body imaging applications.[1] At the same time, the interior microenvironment of ferritin allows only certain sized Au clusters to form, and clusters cannot grow larger than ~1 nm in diameter (Figure 2) under the current experimental conditions. The photoluminescence quantum yield of the far-red Au−Ft was about 8.2% (calibrated with rhodamine 6G using a 470 nm laser), which is higher than the yield reported in the literature.[15]

To characterize the Au nanostructures, we used far-red Au−Ft as an example due to its desirable fluorescence emission properties. Various electron microscopic techniques were used to characterize the complexes, including cryo-electron microscopy (Cryo-EM), high-angle annular dark-field scanning transmission electron microscopy (HAADF-STEM), and high-resolution TEM (HRTEM). Cryo-EM was used to directly observe the size and distribution of Au clusters and the ferritin proteins. Although image contrast was low due to the low-dose imaging conditions, cryo-EM images showed the structural integrity of the ferritin nanoreactors, as indicated by the correct shape and dimension of ferritin particles (Figure 2a). More importantly, pairs of Au clusters were found to localize inside ferritin nanoreactors in many cases (Figure 2a). HAADF-STEM was used to confirm these observations and to obtain a precise distance measurement between the pairs of Au clusters in the protein nanoreactors. Pairs of Au clusters were consistently observed in close proximity (Figure 2b, indicated by ovals), with a maximal $X-Y$ plane projection distance of 6 nm in most cases (Figure 2b). The average distance between the paired Au clusters is about 3.5 nm (shown in Figure S2a). These observations clearly indicate that Au clusters exist as pairs in ferritin nanoreactors. Additional energy-dispersive-X-ray spectroscopy (EDX) experiments confirmed the presence of elemental Au, but not iron in the Au−Ft samples (Figure 2c). Using HRTEM, paired Au clusters within several nanometers of each other were again observed (Figure 2d), and a typical gold crystalline lattice (spacing 0.22 nm, (111) face) was confirmed (Figure 2d, inset). The average size of the Au clusters is about 1.2 nm (shown in Figure S2b). Finally, the grid used in HAADF-STEM imaging was also observed on an FEI Tecnai F20 TWIN electron microscope equipped with a Gatan 4k × 4k CCD camera at a nominal magnification of 62 000×, and once more paired Au clusters in close proximity were observed (Figure 2e).

We next examined the feasibility of using far-red Au−Ft as a fluorescent probe for both in vitro and in vivo imaging, with the ability of ferritin to target certain cells and tissues. At the cellular level, we chose a human colorectal carcinoma cell line, Caco-2, to assess the efficacy of Au−Ft as a fluorescent probe for cellular imaging as these cells express a ferritin receptor on their plasma membrane.[34] A human hepatoma cell line HepG2 does not express a ferritin receptor expression and was used as a negative control. The Caco-2 cells were incubated with 500 nM Au−Ft fluorescent probe for 12 h, and significant uptake of the complex was observed. The probe localized mainly to the plasma membrane, but a few stained membrane vesicles were also observed (Figure 3a). In contrast, no obvious fluorescence signal was detectable in ferritin receptor negative HepG2 cells (Figure 3b) under the same experimental conditions. These experiments confirm that Au−Ft clusters are able to be used as fluorescent probes at the cellular levels and suggest the cellular uptake is mediated mainly by specific ferritin receptors. Thus, Au−Ft nanostructures have the potential to target specific cell types that express ferritin receptors.

Cytotoxicity studies of far-red Au−Ft indicated that neither apoFt nor Au−Ft had adverse effects on Caco-2 (Figure 3c) or HepG2 cell viability (Figure 3d) up to a concentration of 10 μM concentration. These results showed that Au−Ft has no or very low cytotoxicity, an important characteristic for an agent with a potential application in live animal imaging.

To evaluate far-red Au−Ft as an agent for in vivo imaging, we carried out whole-body fluorescent imaging studies in nu/nu (nude) female mice. Animals were injected via a lateral tail vein with 0.8 nmol/g body weight Au−Ft. Dorsal fluorescence signals were recorded at different time points with a Maestro in vivo optical imaging system. Spectral unmixing using the pure autofluorescence and Au−Ft spectra yielded a superimposed image. The fluorescence intensity of the unmixed Au−Ft was analyzed, and 30 min after injection, a kidney-like shape was observed on each side of the spine as indicated by the arrows in Figure 4a. The fluorescent signals reached the highest intensity 3−5 h after injection and could be observed for up to at least 7 h. According to studies exploring the size-dependent biodistribution of nanoparticles for kidney accumulation, nanoparticles with a diameter less than 20 nm indeed could be found in kidney.[35−37] However, very few studies showed significant nanoparticle accumulation in kidney.[37] Meanwhile, a cutoff size for efficient kidney excretion of nanoparticles is approximately 5.5 nm.[38] In the current study, our nanostructures with approximately 12 nm in diameter have shown significant fluorescence localized in both kidneys. This observation suggests that a specific uptake mechanism needs to be involved for the kidney targeting of Au−Ft. It has been reported that certain cell types in the kidneys are able to bind ferritin, implying that ferritin receptors are present and involved in the kidney uptake of ferritin. For example, proximal tubule cells have been shown to bind ferritin,[39−41] and a receptor for L-subunit ferritin, Scara5, has been identified in the kidney during the nephrogenesis.[42] The clear kidney targeting of Au−Ft is consistent with the expression of ferritin receptors in this organ. In addition to the likely kidney fluorescence, strong signals were also observed in the

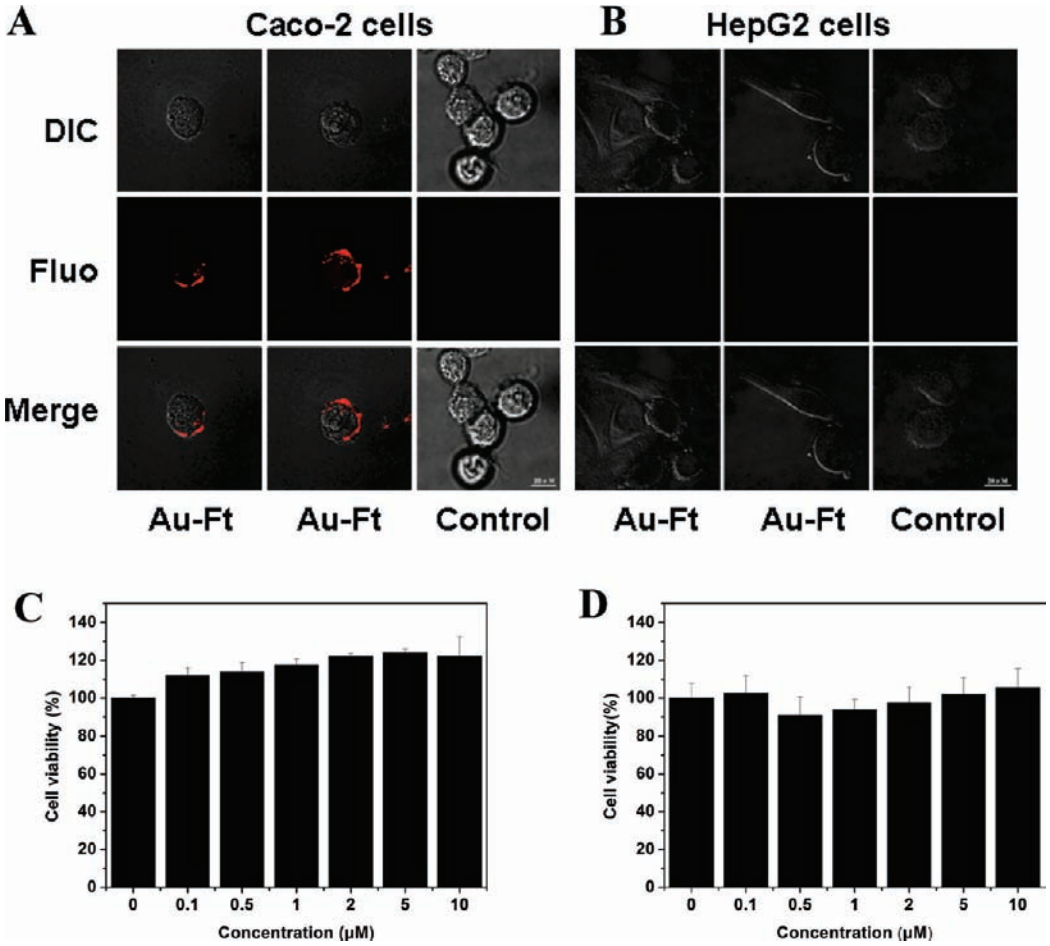

Figure 3. In vitro imaging of the paired far-red Au−Ft and cytotoxicity assays. (a) Receptor-mediated cellular binding and uptake of far-red Au−Ft in Caco-2 cells. Cells were cultured in Au−Ft containing medium (500 nM) on 35 mm glass coverslips for 12 h and subsequently examined using confocal microscopy. Differential interference contrast (DIC) images of cell morphology are shown in the first row. Confocal images of cells treated with Au−Ft fluorescent probe showing distribution of Au−Ft are in the second row. The bottom row is an overlay of the first two rows. Scale bar = 20 μm. (b) No apparent cellular uptake of far-red Au−Ft was observed in HepG2 cells. Experimental details were as described in (a). No obvious effects of Au−Ft on cell viability in either Caco-2 (c) or HepG2 cells (d) were observed. Cell viability (the number of viable cells expressed as a percentage of the total cell number) was measured using a Vi-CELL XR Cell Viability Analyzer. These experiments were performed in triplicate. Results are representative of three independent experiments. Error bars represent standard deviations.

central dorsal region, possibly emanating from the liver and spleen. However, due to the expression of ferritin binding proteins identified in liver,[43] it is possible that receptor-mediated uptake of Au−Ft partially accounts for the strong emission of the fluorescent dye. Therefore, these signals are likely due to the combined effects of accumulation in liver area, that is, the clearance of Au−Ft from the body through the reticuloendothelial system[44,45] and the receptor-mediated uptake.

To confirm the in vivo imaging results, various organs were excised for ex vivo imaging (Figure 4b and c). Under the same fluorescent excitation conditions as those used for whole animals, the strongest signals were associated with the liver and kidney as compared to the control organs from animals injected with saline (Figure 4b). To investigate the dynamic changes of the Au−Ft signal over time, various organs were excised, and their fluorescence signals were recorded at different time intervals after Au−Ft injection. Again, as shown in Figure 4c, kidney and liver showed the strongest fluorescence signals, and the specific signals last for at least 6−7 h. Other organs such as the spleen also showed moderate signal; however, the signal disappeared from the organ very quickly (within 2 h) (Figure 4c).

To confirm the kidney-specific targeting of Au-Ft, the unmixing fluorescence spectra of kidney and lung were also recorded with a Nuance optical system (CRi, Woburn, USA) at the tissue levels. As shown in Figure 4d, specific red fluorescence signals could be seen in the kidney tissue section, mostly localized around proximal tubule cells. This is similar to the distribution patterns shown by the L-ferritin receptor Scara5.[42] In contrast, no specific fluorescence signal could be seen in the lung tissue. To further analyze the distribution of the far-red Au−Ft probe in the kidney, the nuclei were stained with DAPI (green). As shown in Figure 4e, strong Au−Ft (red) fluorescence existed in both renal cortex (marked by the glomerulus) and renal medulla (marked by the renal tubular), and Au−Ft could be found in the plasma of kidney cells in both sections. In contrary, no specific Au−Ft fluorescence signal could be seen in the kidney tissue slides from the mice without Au−Ft administration.

To quantify the tissue distribution of the far-red Au−Ft complexes, inductively coupled plasma mass spectrometry (ICP-MS) was used to measure elemental Au levels in various organs of mice injected with the same amount of Ft−Au as in the imaging experiments. As shown

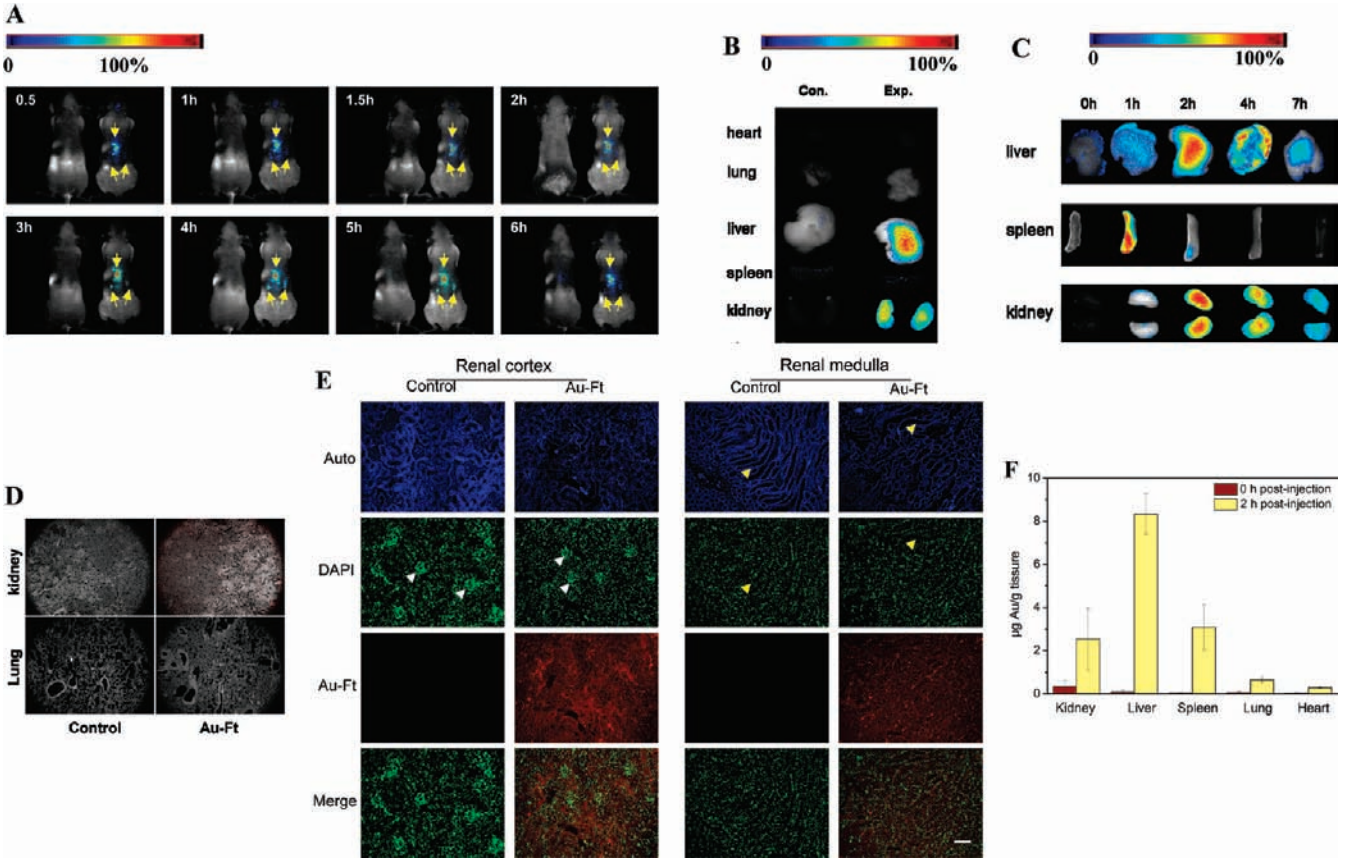

Figure 4. In vivo and ex vivo imaging of far-red Au−Ft with female nude mice and ICP-MS analysis showing the distribution of Au in various tissues. (a) Whole body dorsal fluorescence images of nu/nu female mice at different time points after far-red Au−Ft injection into the tail vein. The final concentration of Au−Ft was 0.8 nmol/g body weight. For each panel, the Au−Ft injected mouse is shown on the right and a saline injected control is shown on the left. Ex vivo imaging of Au−Ft in mouse organs (b and c). (b) Fluorescence images of nu/nu female mouse organs 6 h after Au−Ft injection. Control mice were injected with physiological saline, and organs from these animals are shown on the left. (c) Fluorescence images of nu/nu female mouse organs at different time points after Au−Ft tail vein injection. The final concentration of far-red Au−Ft was 0.8 nmol/g body weight. Tissue distribution of far-red Au−Ft in both kidney and lung in Au−Ft injected mice or the control mice (d and e). (d) Organ distribution of far-red Au−Ft in both kidney and lung of Au−Ft injected mice or the control mice. (e) The detailed tissue distribution in kidney of Au−Ft injected and control mice. The first row showed the tissue background fluorescence (autofluorescence), which indicated the kidney tissue structure. The distribution of Au−Ft fluorescent probe in different kidney regions was shown in the second row. The DAPI staining in the third row indicated the nuclei of kidney tissue. The bottom row was an overlay of the second and third rows. The white arrow showed the glomerulus, and the yellow arrow showed the renal tubular. Scale bar = 200 μm. (f) ICP-MS analysis showing the distribution of Au and specific tissue accumulation in various tissues at 2 h after injection of Au−Ft. Kidney and liver are the major sites of Au accumulation.

in Figure 4f, consistent with the fluorescent imaging results, liver, kidney, and spleen were the major target tissues of Au−Ft 2 h postinjection. Lung and heart had very low levels of Au. Together, the in vivo imaging and Au elemental distribution studies demonstrate that Au−Ft can be used as a fluorescent probe for live animal imaging, particularly for targeting the kidney and liver. These studies also indicate feasibility of living animal imaging with the enhanced paired Au clusters in protein nanoreactors. The biocompatible far-red fluorescence probe provides very good tissue penetration, an essential characteristic for live animal imaging studies.

■ CONCLUSIONS

The far-red and near-infrared photoluminescence intrinsic to noble metal clusters (such as gold, Au and silver, Ag) is ideal for biological imaging due to its deep tissue penetration, high biocompatibility, and low cytotoxicity. Ferritins are native nanoscale structures with unique, defined three-dimensional structures and biological functions. In our current study, we used horse spleen ferritin, which contains mainly L-ferritin subunits, as a nanoreactor to direct the synthesis of a biocompatible nanostructure. The integration of noble metal clusters and proteins enables the generation of novel nanostructures with great potential for biomedical applications. We have successfully synthesized various paired Au clusters with tunable fluorescent emissions, from green to far-red, under the "points of control" strategy. The resulting Au−Ft complex showed significantly enhanced fluorescence intensity and a red shift in the maximal emission wavelength as compared to single Au clusters. These observations directly support the proposal that FRET effects indeed occurred between clusters. We also identified the critical distance (6 nm) between the pairs of Au clusters to allow FRET to occur. Furthermore, both in vitro and in vivo, we achieved ferritin receptor-mediated targeting and biomedical imaging with far-red Au−Ft. Our study demonstrates that Au−Ft can be an excellent fluorescent probe for whole body imaging with particular targeting to the kidney. In

dx.doi.org/10.1021/ja200746p |J. Am. Chem. Soc. 2011, 133, 8617–8624

summary, the "points of control" strategy may provide a general route for the controlled of clusters of noble metal atoms of very small size (less than 1 nm) within low toxicity and bioactive nanostructures. The combination of the properties of biomolecules and inorganic materials paves the way for the synthesis of various novel nanobiostructures for biomedical applications.

■ ASSOCIATED CONTENT

Supporting Information. Figures S1 and S2. This material is available free of charge via the Internet at http://pubs.acs.org.

■ AUTHOR INFORMATION

Corresponding Author

niegj@nanoctr.cn; xuli@jlu.edu.cn; zhaoyuliang@ihep.ac.cn

Author Contributions

#These authors contributed equally.

■ ACKNOWLEDGMENT

This work was supported by grants from MOST 973 (2011-CB933400, 2010CB933600, 2010CB912400) and NSFC (1097-9011; 30900278; 31000452). G.N. gratefully acknowledges the support of the Chinese Academy of Sciences, Hundred Talents Program. We thank Professor Xiaochun Wu for reviewing the manuscript and Ms. Ying Qu for help with XAFS experiment.

■ REFERENCES

(1) Gao, X. H.; Cui, Y. Y.; Levenson, R. M.; Chung, L. W. K.; Nie, S. M. *Nat. Biotechnol.* **2004**, *22*, 969.
(2) de la Rica, R.; Matsui, H. *Chem. Soc. Rev.* **2010**, *39*, 3499.
(3) Rosi, N. L.; Mirkin, C. A. *Chem. Rev.* **2005**, *105*, 1547.
(4) Zheng, J.; Nicovich, P. R.; Dickson, R. M. *Annu. Rev. Phys. Chem.* **2007**, *58*, 409.
(5) Lin, C. A.; Yang, T. Y.; Lee, C. H.; Huang, S. H.; Sperling, R. A.; Zanella, M.; Li, J. K.; Shen, J. L.; Wang, H. H.; Yeh, H. I.; Parak, W. J.; Chang, W. H. *ACS Nano* **2009**, *3*, 395.
(6) Yoon, B.; Hakkinen, H.; Landman, U.; Worz, A. S.; Antonietti, J. M.; Abbet, S.; Judai, K.; Heiz, U. *Science* **2005**, *307*, 403.
(7) Turner, M.; Golovko, V. B.; Vaughan, O. P. H.; Abdulkin, P.; Berenguer-Murcia, A.; Tikhov, M. S.; Johnson, B. F. G.; Lambert, R. M. *Nature* **2008**, *454*, 981.
(8) Wu, X.; He, X. X.; Wang, K. M.; Xie, C.; Zhou, B.; Qing, Z. H. *Nanoscale* **2010**, *2*, 2244.
(9) Yadav, B. D.; Kumar, V. *Appl. Phys. Lett.* **2010**, 97.
(10) Wu, Z. K.; Lanni, E.; Chen, W. Q.; Bier, M. E.; Ly, D.; Jin, R. C. *J. Am. Chem. Soc.* **2009**, *131*, 16672.
(11) Zhu, M.; Lanni, E.; Garg, N.; Bier, M. E.; Jin, R. *J. Am. Chem. Soc.* **2008**, *130*, 1138.
(12) Tang, Z. H.; Xu, B.; Wu, B. H.; Germann, M. W.; Wang, G. L. *J. Am. Chem. Soc.* **2010**, *132*, 3367.
(13) Shichibu, Y.; Negishi, Y.; Tsukuda, T.; Teranishi, T. *J. Am. Chem. Soc.* **2005**, *127*, 13464.
(14) Gruene, P.; Rayner, D. M.; Redlich, B.; van der Meer, A. F. G.; Lyon, J. T.; Meijer, G.; Fielicke, A. *Science* **2008**, *321*, 674.
(15) Xie, J.; Zheng, Y.; Ying, J. Y. *J. Am. Chem. Soc.* **2009**, *131*, 888.
(16) Harrison, P. M.; Arosio, P. *Biochim. Biophys. Acta* **1996**, *1275*, 161.
(17) Arosio, P.; Ingrassia, R.; Cavadini, P. *Biochim. Biophys. Acta* **2009**, *1790*, 589.
(18) Herrero, M. A.; Guerra, J.; Myers, V. S.; Gomez, M. V.; Crooks, R. M.; Prato, M. *ACS Nano* **2010**, *4*, 905.
(19) Knecht, M. R.; Garcia-Martinez, J. C.; Crooks, R. M. *Langmuir* **2005**, *21*, 11981.
(20) Ueno, T.; Abe, M.; Hirata, K.; Abe, S.; Suzuki, M.; Shimizu, N.; Yamamoto, M.; Takata, M.; Watanabe, Y. *J. Am. Chem. Soc.* **2009**, *131*, 5094.
(21) Ueno, T.; Suzuki, M.; Goto, T.; Matsumoto, T.; Nagayama, K.; Watanabe, Y. *Angew. Chem., Int. Ed.* **2004**, *43*, 2527.
(22) Jin, Y.; Gao, X. *Nat. Nanotechnol.* **2009**, *4*, 571.
(23) Crooker, S. A.; Hollingsworth, J. A.; Tretiak, S.; Klimov, V. I. *Phys. Rev. Lett.* **2002**, 89.
(24) Koole, R.; Liljeroth, P.; Donega, C. D.; Vanmaekelbergh, D.; Meijerink, A. *J. Am. Chem. Soc.* **2006**, *128*, 10436.
(25) Nie, Z. H.; Petukhova, A.; Kumacheva, E. *Nat. Nanotechnol.* **2010**, *5*, 15.
(26) Wargnier, R.; Baranov, A. V.; Maslov, V. G.; Stsiapura, V.; Artemyev, M.; Pluot, M.; Sukhanova, A.; Nabiev, I. *Nano Lett.* **2004**, *4*, 451.
(27) Welsher, K.; Liu, Z.; Sherlock, S. P.; Robinson, J. T.; Chen, Z.; Daranciang, D.; Dai, H. *Nat. Nanotechnol.* **2009**, *4*, 773.
(28) Grabolle, M.; Spieles, M.; Lesnyak, V.; Gaponik, N.; Eychmuller, A.; Resch-Genger, U. *Anal. Chem.* **2009**, *81*, 6285.
(29) Skibsted, L. H.; Bjerrum, J. *Acta. Chem. Scand., Ser. A* **1977**, *31*, 155.
(30) Skibsted, L. H.; Bjerrum, J. *J. Indian Chem. Soc.* **1977**, *54*, 102.
(31) Negishi, Y.; Nobusada, K.; Tsukuda, T. *J. Am. Chem. Soc.* **2005**, *127*, 5261.
(32) Chen, C.; Bobisch, C. A.; Ho, W. *Science* **2009**, *325*, 981.
(33) Yan, F.; Zhang, Y.; Yuan, H. K.; Gregas, M. K.; Vo-Dinh, T. *Chem. Commun.* **2008**, 4579.
(34) Kalgaonkar, S.; Lonnerdal, B. *J. Nutr. Biochem.* **2009**, *20*, 304.
(35) De Jong, W. H.; Hagens, W. I.; Krystek, P.; Burger, M. C.; Sips, A. J. A. M.; Geertsma, R. E. *Biomaterials* **2008**, *29*, 1912.
(36) Kumar, R.; Roy, I.; Ohulchanskky, T. Y.; Vathy, L. A.; Bergey, E. J.; Sajjad, M.; Prasad, P. N. *ACS Nano* **2010**, *4*, 699.
(37) Lu, M. G.; Al-Jamal, K. T.; Kostarelos, K.; Reineke, J. *ACS Nano* **2010**, *4*, 6303.
(38) Choi, H. S.; Liu, W.; Liu, F.; Nasr, K.; Misra, P.; Bawendi, M. G.; Frangioni, J. V. *Nat. Nanotechnol.* **2010**, *5*, 42.
(39) Dimmock, E.; Franks, D.; Glauert, A. M. *J. Cell Sci.* **1972**, *10*, 525.
(40) Grinnell, F.; Hays, D. C. *Anal. Biochem.* **1979**, *97*, 400.
(41) Maunsbach, A. B. *J. Ultrastruct. Res.* **1966**, *16*, 1.
(42) Li, J. Y.; Paragas, N.; Ned, R. M.; Qiu, A. D.; Viltard, M.; Leete, T.; Drexler, I. R.; Chen, X.; Sanna-Cherchi, S.; Mohammed, F.; Williams, D.; Lin, C. S.; Schmidt-Ott, K. M.; Andrews, N. C.; Barasch, J. *Dev. Cell* **2009**, *16*, 35.
(43) Wang, W.; Knovich, M. A.; Coffman, L. G.; Torti, F. M.; Torti, S. V. *Biochim. Biophys. Acta* **2010**, *1800*, 760.
(44) Mouli, S. K.; Zhao, L. C.; Omary, R. A.; Thaxton, C. S. *Nat. Rev. Urol.* **2010**, *7*, 84.
(45) Petros, R. A.; DeSimone, J. M. *Nat. Rev. Drug Discovery* **2010**, *9*, 615.